

# NEXAFS and MS-AES spectroscopy of the C 1s and Cl 2p excitation and ionization of chlorobenzene

## Production of dicationic species

**Coutinho, Lúcia H.; Ribeiro, Fabio de A.; Tenorio, Bruno N. C.; Coriani, Sonia; Dos Santos, Antonio C. F.; Nicolas, Christophe; Milosavljevic, Aleksandar R.; Bozek, John D.; Wolff, Wania**

*Published in:*
Physical Chemistry Chemical Physics

*Link to article, DOI:*
10.1039/d1cp03121j

*Publication date:*
2021

*Document Version*
Peer reviewed version

PCCP

ARTICLE TYPE

Cite this: DOI: 00.0000/xxxxxxxxxx

# NEXAFS and MS-AES spectroscopy of the C $1s$ and Cl $2p$ - excitation and ionization of chlorobenzene: production of dicationic species

Lúcia H. Coutinho*[a], Fabio de A. Ribeiro[b], Bruno Tenorio[c], Sonia Coriani[c], Antonio C. F. dos Santos[a], Christophe Nicolas[d], Aleksandar Milosavljevic[d], John Bozek[d] and Wania Wolff*[a]

Received Date
Accepted Date

DOI: 00.0000/xxxxxxxxxx

We report on the single- and double-charge photofragment formation by synchrotron radiation, following C $1s$ core excitation and ionization and Cl $2p$ inner excitation and ionization of chlorobenzene, $C_6H_5Cl$. From a comparison of experimental near-edge X-ray absorption fine structure spectra and theoretical *ab initio* calculations, the nature of various core and inner shell transitions of the molecule and pure atomic features were identified. To shed light on the normal Auger processes following excitation or ionization of the molecule at the Cl $2p$ or C $1s$ sites, we addressed the induced ionic species formation. With energy resolved electron spectra and ion time-of-flight spectra coincidence measurements, the ionic species were correlated to binding energy regions and initial states of vacancies. We explored the formation of the molecular dication $C_6H_5Cl^{2+}$, the analogue benzene dication $C_6H_4^{2+}$, and the singly charged species produced by single loss of carbon atom, $C_5H_nCl^+$. The appearance and intensities of the spectral features associated with these ionic species are shown to be strongly site selective and dependent on the energy ranges of the Auger electron emission. Unexpected intensities for the analogue double charged benzene $C_6H_4^{2+}$ ion were observed with fast Auger electrons. The transitions leading to $C_6H_5Cl^{2+}$ were identified from the binding energy representation of high resolution electron energy spectra. Most of $C_6H_5Cl^{2+}$ ions decay into two singly charged moieties, but intermediate channels are opened leading to other heavy dicationic species, $C_6H_4^{2+}$ and $C_6H_4Cl^{2+}$, the channel leading to the first of these being much more favored than the other.

## 1 Introduction

The application of sophisticated, state-of-the-art theoretical and experimental spectroscopic methods is continuously improving our understanding of the electron and ion spectra of complex molecules. Photoelectron (PES), Auger electron (AES), Near Edge X-ray Absorption Fine Structure (NEXAFS), Near-edge X-ray Absorption Mass Spectrometry (NEXAMS), and ion Time-Of-Flight spectroscopy (TOF-MS) can provide detailed information on the molecular electronic structure and dissociation mechanisms.[1]

The dependence of the fragmentation pattern and mechanism on the site of the core and inner ionization/excitation has been investigated by several groups in recent years. Site-selective dissociation upon core and inner shell ionization has been observed from small to large size open-chain organic molecules[2–18] as well as from more complex, biologically relevant, cyclic organic species.[19–31] Some of these studies explained the observed site-selective fragmentation patterns by the excess energy available in the dicationic final state after Auger decay.[6,8,15,20–24] Other studies identified the site-selective dissociation through the fragmentation yields of ions as a function of the photons' energies, scanning across core ionization energies.[30–32] By means of NEXAMS on $C_{27}H_{3}6N_5O_7S$, the fragmentation yields of ionic species induced by resonant and nonresonant absorption at the sulfur $L$-edge have been obtained.[31] Recent investigations of the site-specificity in small molecules such as formamide, $XeF_2$ and acetylene dication were conducted at X-ray free-electron laser facilities using the high temporal resolution of X-ray pump-probe spectroscopy, where transient dynamics could be followed through the intermediate states.[16–18] Here, we have quantitatively evaluated site-specificity aspects of singly and doubly-charged photoions, by a combination of NEXAFS, coincident AES and TOF-MS. The prediction of hetero-site-specificity in species formation remains challenging.

In the case of aromatic and heteroaromatic molecules, measurements at the C, N, and O $K$-edges were directed to exploit

[a] Physics Institute, Federal University of Rio de Janeiro, Rio de Janeiro, 21941-972, Brazil
[b] Federal Institute of Rio de Janeiro, Rio de Janeiro, 26530-060, Brazil
[c] Department of Chemistry, Technical University of Denmark, Kongens Lyngby, 2800, Denmark
[d] Synchrotron SOLEIL, Gif-sur-Yvette, 91192, France
* E-mail: lucia@if.ufrj.br, wania@if.ufrj.br

site-selectivity of the core excitation on pyrimidine, purine and phenol molecules.[22,23,30,32–34] Branching ratios of the major fragment ions of pyrimidine ($C_6H_4N_2$), purine ($C_5H_4N_4$) and phenol ($C_6H_5OH$) as a function of photon energy at the carbon, nitrogen and oxygen *K*-edge were obtained from the curves of intensity variation divided by the Total Ion Yield (TIY) NEXAFS spectra.[30,32] The C and N Resonant Auger Electron (RAE) spectra of pyrimidine were measured at selected photon energies.[33,34] The binding energy scale representation reported in these studies has allowed a comparison of the final state population depending on the intermediate state and the identification of the contribution of the resonant Auger decay.

Here, we extend the previous works on benzene and benzene derivatives[35,36] and report an investigation aimed at the site-selectivity of molecular fragmentation and formation of chlorobenzene metastable dications. In this context, complex competitions in species formation and production in aromatic substituted benzene among the carbon 1*s* electrons and the 2*p* electrons of the substituent atom, may be highlighted in resonant and normal Auger decay processes. Choosing a photon energy above core/inner shell excitation and C 1*s* and Cl 2*p* ionization thresholds, we access normal Auger effect that can reveal differences in the population of the excited states and post fragment ion formation. Here, using an energy-resolved electron and ion coincidence technique coupled to TIY NEXAFS spectra, we selected the halobenzene molecule chlorobenzene to investigate the formation of ionic species, with emphasis on metastable dicationic species, via C 1*s* and Cl 2*p* normal Auger processes.

NEXAFS spectra proved essential in order to identify the origins of the excited core/inner-shell electrons and the corresponding destination orbitals.[19,32,37] The C 1*s* and Cl $2p_{3/2}$ and Cl $2p_{1/2}$ Auger decay processes of chlorobenzene in the NEXAFS spectra, as well as in the electron energy spectrum, have not been discussed up to now. Assignment of the energetic ordering and character of these excited states is often hampered by features resulting from different states with similar binding energies. Only from electronic structure calculations used as guidance for the interpretation of these excited states it is possible to clarify the electron motions triggered by Auger decay. In the present study, a combined theoretical and experimental approach was mandatory. Accurate theoretical NEXAFS spectra at the carbon *K*-edge and chlorine *L*-edge have been obtained within the multi-state restricted active space perturbation theory of second order (MS-RASPT2) approximation.[38,39] By means of the correlation between the electrons' kinetic energy and the derived binding energy, the main goal of this report is to investigate the formation of particular singly and doubly charged molecular ionic species dependent on the core and inner-shell ionization, and to identify the dissociation processes and energy limits imposed on the fragments' formation. The C 1*s* and Cl 2*p* ionization with Auger electron emission surely restrains particular conditions on the molecular species formation and dissociation with a single carbon or chlorine atom loss.

The formation of molecular single and double charged species of chlorobenzene under the predominance of Auger processes raises several questions: Can ionized/excited molecular single-hole (1*h*) transitions lead to chlorobenzene dications or analogue benzene dications? Is the formation of molecular dications more strongly prompted by core ionization of the ring carbon atoms, or by inner-shell ionization of the halogen chlorine atom? Are the dications' intensities more pronounced in normal or in resonant Auger processes? Is the dications' formation correlated to the emission of fast or slow Auger electrons? In this context, we decided to dedicate the present work mainly to the normal Auger process and focus on the influence of the C 1*s* core excitation and ionization and Cl 2*p* inner-shell excitation and ionization on the dications formation. A further report will follow dedicated to the resonant Auger processes, where more experimental measurements are needed.

Therefore, novel aspects concerning the production of ionic species were revealed as correlated to the normal Auger electron emission after ionization from C core and Cl inner-shell orbitals. As a result of the Auger process that is driven by electron correlation we observed differentiated single- and double-charged molecular species production.

As anticipated, we present energy-resolved electron spectra taken in coincidence with ion- time-of-flight spectra of chlorobenzene correlated to normal C 1*s* and Cl 2*p* Auger processes. Following recent laboratory studies on halobenzene molecular dications[40], we investigate how photo activation influences the formation of the molecular dication $C_6H_5Cl^{2+}$ and the dication analogue to benzene $C_6H_4^{2+}$, and compare them to fragments produced by single loss of carbon atom, $C_5H_nCl^+$. The appearance of these ionic species as well as their spectral intensities are shown to be strongly dependent on the atom site and the energy ranges of the emitted Auger electrons. From the high-resolution Auger spectra, we discriminated the binding energy regions for several molecular states and could identify the transitions leading to $C_6H_5Cl^{2+}$. While high kinetic energy electrons (low binding energies) are correlated to the dication $C_6H_5Cl^{2+}$, the electrons of doubly charged benzene analogue $C_6H_4^{2+}$ appear already shifted in energy. The singly-charged ions resulting from fragmentation are mostly associated to Auger electrons emitted at the low kinetic energy range. In particular, the site selectivity of the dications' production was addressed. For the doubly charged benzene analogue $C_6H_4^{2+}$, unexpected intensities were observed and with comparable intensity to the $C_6H_5Cl^{2+}$ after the Cl 2*p* edge (inner shell ionization). Other dications, such as the dication where an additional hydrogen atom has been removed, $C_6H_4Cl^{2+}$, and the dication analogue to phenyl, $C_6H_5^{2+}$, show faint intensities.

The manuscript is divided in four sections. The experimental section shortly describes the setups used in the experiments. The calibration procedures and parameters are presented in more detail as well as the spectral energy ranges selected for the measurements. The following section presents the computational details of the quantum mechanical calculations used to clarify some features of the spectra. The results and analysis section follows and is divided in two subsections dedicated to the techniques employed: (1) NEXAFS spectroscopy, and (2) Normal Auger spectroscopy. At the end we present a resumé and conclusions.

## 2 Experimental section

The experiments were performed at the synchrotron radiation facility SOLEIL, on the ultra high resolution soft X-ray beamline PLÉIADES (Polarized Light source for Electron and Ion Analysis from Diluted Excited Species).[41] The 80 mm period permanent magnet APPLE-II type undulator delivered photons with linear vertical polarization and energies in the Cl $2p$ and C $1s$ domains, selected by a PGM monochromator. Three stations mounted sequentially across the beamline were used, the EPICEA multicoincidence setup, the R4000 hemispherical electron analyzer from VG Scienta, and an ionization chamber for NEXAFS measurements.

The experiments done at the EPICEA setup recorded electrons and fragment ions in coincidence, which were fully momentum analysed.[42] The electrons were energy-analyzed using a double toroidal analyzer (DTA) coupled to four conical lenses, which ensured an electron energy resolution of 0.5-0.8 % of the analyzer pass energy, with a collection efficiency of about 4.2 % of 4 $\pi$. The width of the electrons' kinetic energy window is about 12 % of the pass energy.[43] Two different configurations for the DTA were used depending on the investigated energy region, one with pass energy of 120 eV and kinetic energy of 177 eV for the Cl $2p$ Auger electrons, and the other with 210 eV pass energy and 270 eV kinetic energy for the C $1s$ Auger electrons. The calibration of the DTA was performed by measuring the Ar $2p$ doublet lines in both configurations.[44] In the direction opposite to the DTA, a 3D focusing ion time-of-flight (TOF) spectrometer measured the resulting fragment ions over the full $4\pi$. The extraction of the ions was triggered by the first detected electron and operated in pulsed mode to maintain the kinetic energy resolution of the electrons before their detection at the DTA. The fortuitous coincident events created by ions coming from uncorrelated electrons were afterwards subtracted by software from the coincident spectra by systematically measuring ion signals with randomly timed electrostatic extraction pulses. A delay line anode detector measured the time and position of the ions, allowing the correlation of the momentum of the ion(s) with the energy ranges of the emitted electrons. With this configuration, Energy Selected Auger Electron PhotoIon COincidence spectra (ES-AEPICO) were generated by recording the cationic molecular fragments in coincidence with energy-selected Auger electrons. The mass/charge ion calibration was done with $Ar^{2+}$ and $Ar^{3+}$ TOF peaks.

With the hemispherical electron energy analyzer (VG Scienta R4000) mounted perpendicular to the propagation axis of the photon beam, high resolution kinetic energies of the Auger electrons emitted by chlorobenzene were collected. Normal Auger electrons in the energy domains of chlorine $2p$ and carbon $1s$ edges with kinetic energies of 166–183 eV and 236–273 eV, respectively, were scanned with 40 meV step size using 350 eV photons. The analyzer was used with a constant pass energy of 100 eV and 125 meV resolution. It is to note that the lower resolution of the EPICEA coincidence measurements reproduces very well the overall shape of the Auger distributions measured by the high resolution VG Scienta analyzer. The high resolution electron spectra were essential to identify with precision the C $1s$ and Cl $2p$ transitions and, furthermore, to select the Auger-electron energy regions in the DTA spectra. These regions were used to extract the ion species formation correlated to the transitions or vice versa.

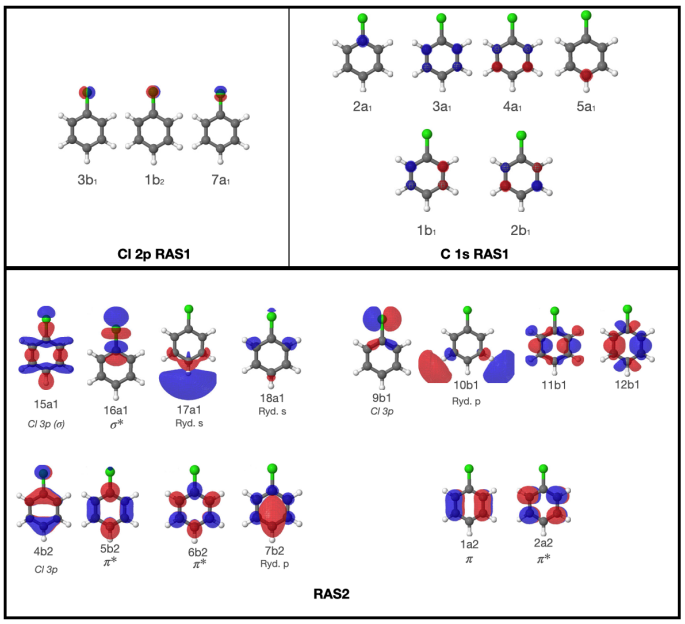


Fig. 1 RASSCF active space for the C1s and Cl $2p$ excited/ionized states. The optimized RASSCF orbitals labeled as Rydberg are plotted with isosurface value set to 0.03, while the remaining ones are plotted with isosurface 0.05.

At the end of the beamline TIY mode, NEXAFS measurements were done at the ionization chamber. Selecting a 5 $\mu$m slit, the synchrotron photon energy was calibrated with an energy resolution $\delta$E of 17.5 m eV using the Ar $2p_{3/2} \rightarrow 4s$ resonance at 244.39 eV.[45] The Ar pressure in the gas cell was set at $1.0 \times 10^{-7}$ mbar and the NEXAFS spectrum was recorded in the range 244.2–248.8 eV with 10 meV steps. The NEXAFS spectra of chlorobenzene were recorded in the Cl $2p$ and C $1s$ energy regions, from 180 to 220 eV and from 265 to 320 eV, respectively, with varying energy steps, as small as 20 meV in the resonances regions. For both spectra, a 5 $\mu$m slit was selected, delivering photons with 12 meV resolution in the Cl $2p$ energy region, and 21 meV resolution in the C $1s$ energy region.

Chlorobenzene is a clear liquid at room temperature, with a mild almond-like odor. Before injection into the experimental chambers, the liquid sample, purchased from Sigma Aldrich with 99.5% purity, was degassed by several freeze-pump-thaw cycles. Its vapor pressure is low enough to produce a residual gas in the experimental chambers. The gas pressure for the EPICEA measurements was maintained around $8 \times 10^{-7}$ mbar, while for the NEXAFS and Scienta experiments it was raised to about 4–6 $\times 10^{-6}$ mbar. Sample pressure, acquisition time and photon flux were monitored continuously during all measurements.

## 3 Computational Details

For the current study, a preliminary comparison of experimental data and calculations available in the literature[46] highlighted the urge for more accurate calculations. For this purpose, we

performed a series of high-level *ab initio* quantum chemical calculations using the state averaged restricted active space self-consistent field (RASSCF)[47–49] method with second-order perturbation correction (RASPT2).[38,39] Core-excited states were obtained using the core-valence separation (CVS) scheme as implemented in OpenMolcas.[50] To grasp the main properties of the inner-shell spectra of chlorobenzene, including contributions from Rydberg states, we employed the relativistic ANO-RCC family of basis sets,[51] specifically, the $6s5p4d3f$ basis on Cl, $3s2p1d$ on H, and $5s4p3d2f$ on C, which are similar in size to quadruple-zeta quality. Douglas-Kroll-Hess scalar relativistic effects up to the second order were incorporated in all our calculations. Spin-orbit coupling (SOC) effects in the inner-shell excitation/ionization of the Cl $2p$ edge were included within the state interaction (RASSI)[52–54] method in the atomic mean field integral approximation. In all calculations, we adopted $C_{2v}$ point group symmetry and the experimental equilibrium geometry obtained form the NIST Chemistry WebBook database.[55]

The active space in a RASSCF calculation is defined through a threefold division of the correlation orbital space, denoted RAS1, RAS2 and RAS3.[48] Here, the active space RAS3 was kept empty. The Cl $2p$ excited/ionized states were obtained with the three Cl $2p$ orbitals in the RAS1 space, and additionally four $a_1$, four $b_1$, four $b_2$, and two $a_2$ valence/virtual orbitals in the RAS2 space. The $a_1$ orbitals of RAS2 consist of the upper valence Cl $3p$, the virtual C–Cl $\sigma^*$, and two additional Rydberg $s$ type orbitals. The $b_1$ orbitals consist of the valence Cl $3p$, and three virtual orbitals with some Rydberg $p$ character. The two $a_2$ orbitals added to the RAS2 space are one upper valence $\pi$ and one virtual $\pi^*$. Finally, the $b_2$ orbitals of RAS2 are the upper valence $\pi$, two virtual $\pi^*$ and one Rydberg orbital with $p$ character. All active RASSCF orbitals are shown in Figure 1.

For the C $K$-edge calculation, the three Cl $2p$ orbitals, shown in Figure 1 in RAS1, were replaced by the six C $1s$ orbitals, namely the $2a_1$, $3a_1$, $1b_1$, $4a_1$, $2b_1$, and $5a_1$ orbitals. The same RAS2 space was used.

Dipole transition amplitudes were computed with the RASSI approach (available in OpenMolcas)[52–54] by state averaging over eight core-excited states of each irreducible representation of the $C_{2v}$ point group symmetry. For the Cl $2p$ edge, singlet and triplet final states were computed to include spin-orbit effects.

## 4 Results and Discussion

### 4.1 Near edge X-ray absorption fine structure (NEXAFS) spectroscopy - Electronic excitation

The normalized NEXAFS spectrum of $C_6H_5Cl$ around the chlorine $L$-edge (Cl $2p$) is shown in Figure 2, where six different bands (electronic transitions) are discernible. These features were deconvoluted with Gaussian lineshapes and their energy positions compared to the results of the RASPT2 calculations. These electronic transitions arise from both Cl $2p_{3/2}$ (dark grey curves) and Cl $2p_{1/2}$ (light grey curves) multiplets. The binding energies calculated for the Cl $2p_{3/2}$ ($L_3$) and Cl $2p_{1/2}$ ($L_2$) orbitals are equal to 206.60 and 208.20 eV, respectively, in agreement to Hitchcock *et al.*[46]. Electronic excitations and binding energies are summarized in Table 1.

The first resonance at 201.49 eV (feature **1**) is attributed to the $2p_{3/2} \rightarrow \sigma^*$ state. Hitchcock and co-workers[46] observed two transitions at 201.50 and 203.15 eV, respectively, and assigned them as two spin-orbit partners probing the Cl $2p \rightarrow \pi^*$ excitation. Even though the first peak at 201.49 eV in Figure 2 almost coincides with their attribution for the Cl $2p_{3/2} \rightarrow \pi^*$ excitation, we did not observe here the same spin-orbit separation of $\sim$1.6 eV with respect to the next closest peak, since no reasonable curve fitting was obtained.

In Ref. 26, it was shown from *ab initio* calculations that the first peak observed on the Cl $K$-edge absorption spectrum of chlorobenzene is due to a Cl $1s \rightarrow \sigma^*$ excitation. There, the Cl $1s \rightarrow \sigma^*$ state (2821.6 eV[26]) was observed around 1 eV below the Cl $1s \rightarrow \pi^*$ state (2822.8 eV[26]) at the Cl $K$-edge. According to the present RASPT2 calculations, the Cl $2p_{3/2} \rightarrow \pi^*$ state is responsible for feature **2** in Figure 2, while peaks **1** and **3** are spin-orbit partners of the Cl $2p \rightarrow \sigma^*$ state. Moreover, the energy separation between the Cl $2p_{3/2} \rightarrow \sigma^*$ and $\pi^*$ states obtained here (see Table 1) is also around 1 eV, similar to what was observed on the chlorobenzene $K$-edge spectrum.[26]

It is noteworthy that features **1** to **6** in the region before the Cl $2p$ ionization threshold in Figure 2 exhibit distinct profiles, that may aid in their identification as molecular or atomic electronic transitions. For instance, features **4** and **6** are narrower than feature **1**, as well as the shoulder on **5**, and no single line shape can fit the region encompassed by features **2** and **3**. Also, we observed an energy separation of 1.61 eV between features **4** (203.44 eV) and **6** (205.05 eV), equivalent to the well known spin-orbit splitting for Cl $2p_{3/2}$ and $2p_{1/2}$ multiplets,[46,56,57] with an area ratio of 1.92 : 1, roughly equal to the 2 : 1 area ratio expected for the Cl $2p_{3/2}$ and $2p_{1/2}$ multiplets. This is in perfect agreement with the RASPT2 assignment of features **4** and **6** as the spin-orbit splitting of the Cl $2p$ transition to the unoccupied atomic-like chlorine $4s$ orbital. Their energy separation and area ratio were used as standards for the deconvolution of Cl $2p \rightarrow 4s$ discrete transitions. Feature **5** in Figure 2 was attributed to the Cl $2p_{3/2}$ to a Rydberg type orbital (204.09 eV).

Figure 3 presents the normalized NEXAFS spectrum of $C_6H_5Cl$ around the carbon $K$-edge (C $1s$). Several bound state transitions appear as convoluted peaks positioned below the ionization potential (IP) energy and also superimposed to the continuum of states. Once again, the main features in the pre-edge region are numbered as **1** to **4**. In order to identify their respective contribution, deconvolution of the inner-shell excitation was performed by nonlinear least-squares fitting to the experimental points. Curve fitting of the resonances using a combination of Gaussian and Lorentzian line shapes was found to give the best agreement with the experimental data, while the continuum of states was approximated by a step function (solid green line, partly shown in Figure 3). The corresponding resonances and the binding energies of the nonequivalent carbon atoms are shown in Tables 1 and 2, respectively.

The C $1s$ NEXAFS spectra of gas-phase $C_6H_5Cl$ and benzene ($C_6H_6$) are very similar when compared below the C $1s$ ionization threshold.[59,60] In the case of $C_6H_6$, the first resonance is a

Table 1 Experimental and theoretical photoabsorption energies ( eV) and electronic transitions attributed for the peaks assigned in the C $1s$ and Cl $2p$ NEXAFS spectra of chlorobenzene (Figures 2 and 3). The calculated oscillator strengths (OS) listed below for Cl were multiplied by $10^2$. The calculated RASPT2 energies have been shifted by $-0.357$ and $-0.204$ eV for the Cl and C, respectively, to better compare with the experimental energies. The TDDFT energies on the carbon edge have been shifted by $+10.75$ eV. For the TDDFT oscillator strengths and assignments, please consult the Supplemental Information. In Ref. 46, $C_2$ is the halogen-bound carbon, and $C_1$ any of the others.

| **Peak** | **Expt.** | **RASPT2** | **OS** | **TDDFT** | **Literature** | | **Assignment** | |
|---|---|---|---|---|---|---|---|---|
| | This work | This work | This work | This work | Ref. 46 | Ref. 58 | This work (RASPT2) | Ref. 46 |
| Carbon $1s$ | | | | | | | | |
| **1** | 285.20 | 285.33 | 0.0757 | 285.33 | 285.1 | 285.0 | C $1s$ $(2b_1, 5a_1) \rightarrow \pi^*(2a_2, 5b_2)$ | $C_1 \rightarrow \pi^*(b_2)$ |
| | | 285.60 | 0.0897 | 285.36 | | | C $1s$ $(1b_1, 5a_1) \rightarrow \pi^*(2a_2, 5b_2)$ | |
| | | | | 285.39 | | | | |
| **1'** | 285.37 | | | | | | | |
| **1"** | 285.65 | | | | | | | |
| **1"'** | 285.81 | | | | | | | |
| **2** | 286.51 | 286.51 | 0.0356 | 286.78 | 286.3 | 286.3 | C $1s$ $(2a_1) \rightarrow \pi^*(5b_2)$ | $C_2 \rightarrow \pi^*(b_2)$ |
| **2'** | 286.61 | | | | | | | |
| **3** | 287.55 | 287.46 | 0.0318 | | 287.3 | 287.3 | C $1s$ $(5a_1) \rightarrow \sigma^*(16a_1)$ | $C_1 \rightarrow 4s$ |
| **4** | 288.32 | 288.09 | 0.0370 | 287.87 | 288.1 | 288.7 | C $1s$ $(2a_1) \rightarrow \sigma^*(16a_1)$ | $C_1 \rightarrow 4p$ |
| Chlorine $2p$ | | | | | | | | |
| | | 201.20 | 0.1003 | | | | $2p_{3/2} \rightarrow \sigma^*(16a_1)$ | |
| **1** | 201.49 | 201.34 | 0.3848 | | 201.50 | | $2p_{3/2} \rightarrow \sigma^*(16a_1)$ | $2p_{3/2} \rightarrow \pi^*(b_2)$ |
| | | 201.44 | 0.5056 | | | | $2p_{3/2} \rightarrow \sigma^*(16a_1)$ | |
| | | 201.50 | 0.1336 | | | | $2p_{3/2} \rightarrow \sigma^*(16a_1)$ | |
| **2** | 202.46 | 202.14 | 0.0631 | | | | $2p_{3/2} \rightarrow \pi^*(5b_2)$ | |
| | | 202.22 | 0.0970 | | | | $2p_{3/2} \rightarrow \pi^*(5b_2)$ | |
| **3** | 202.87 | 202.78 | 0.2834 | | 203.15 | | $2p_{1/2} \rightarrow \sigma^*(16a_1)$ | $2p_{1/2} \rightarrow 4s$ |
| | | 202.85 | 0.4011 | | | | $2p_{1/2} \rightarrow \sigma^*(16a_1)$ | $2p_{1/2} \rightarrow \pi^*(b_2)$ |
| **4** | 203.44 | 203.38 | 0.0645 | | | | $2p_{3/2} \rightarrow 4s(17a_1)$ | |
| | | 203.49 | 0.2065 | | | | $2p_{3/2} \rightarrow 4s(17a_1)$ | |
| | | 203.57 | 0.0398 | | | | $2p_{3/2} \rightarrow 10b_1$ | |
| **5** | 204.09 | 204.58 | 0.0546 | | 204.9 | | $2p_{3/2} \rightarrow 18a_1$ | $2p_{3/2} \rightarrow 3d$ |
| | | | | | | | | $2p_{1/2} \rightarrow 4s, 3d$ |
| **6** | 205.05 | 205.05 | 0.0604 | | 206.3 | | $2p_{1/2} \rightarrow 4s(17a_1)$ | |

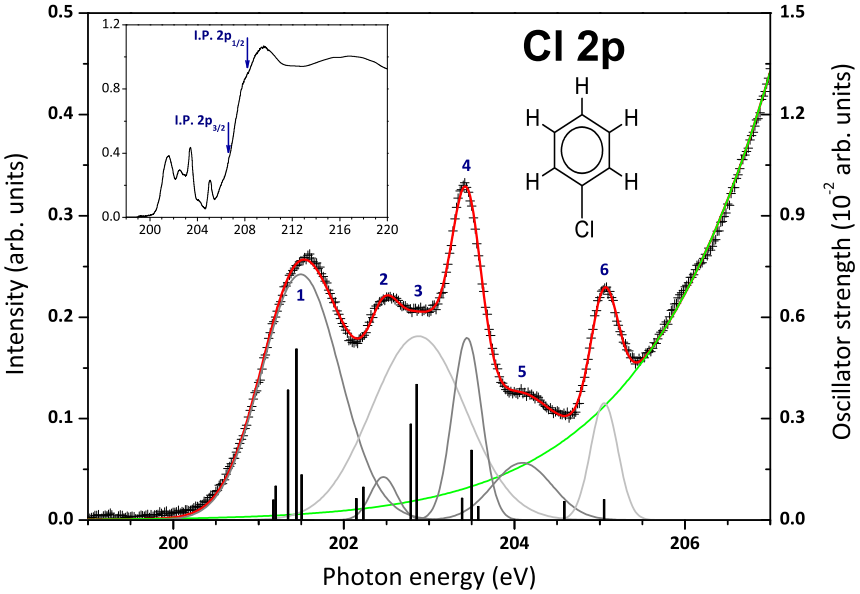


Fig. 2 Normalized Cl *L*-edge (Cl $2p$) NEXAFS spectrum of chlorobenzene ($C_6H_5Cl$) recorded by total ion yield (TIY) detection mode. The features labeled 1 to 6 were deconvoluted with Gaussian line shapes. The electronic transitions from Cl $2p_{3/2}$ are shown as grey curves, whereas those electronic transitions starting from Cl $2p_{1/2}$ are represented by light grey curves. The continuum of states was fitted by an error step function, shown as a green curve. The vertical sticks (solid black) stand for the excitation energies and their respective oscillator strengths computed with the RASPT2 approach. The calculated transitions have been shifted by $-0.204$ eV in order to give a better correspondence with the experimental spectrum. The computed Cl $2p_{3/2}$ and $2p_{1/2}$ ionization edges, respectively, are indicated by the two blue arrows in the inset at top left.

narrow C $1s \rightarrow \pi^*$ transition at ~285 eV[59,61–63] assigned to electron promotion into one of the degenerate unoccupied molecular orbitals of $e_{2u}$ symmetry. As pointed out by Hitchcock and co-workers,[46] the replacement of one hydrogen atom by a chlorine leads to two nonequivalent chemical environments for the carbon atoms in $C_6H_5Cl$. Due to the strong electronegativity of chlorine in the C−Cl bond, the carbon $1s$ binding energy of the halogen-substituted carbon, which corresponds to the C $1s$ $(2a_1)$ orbital in $C_{2v}$ notation, has the highest binding energy, calculated as 291.99 eV. The remaining hydrogen-bearing carbons in the ring at positions 2 to 6 exhibit binding energies ranging from 290.36 to 291.58 eV (see Table 2). For the sake of comparison, we will hereafter use the notation $K_1$ and $K_2$ for the higher (291.99 eV) and lower (290.36 eV) binding energies. Our results are in good agreement with the C $1s$ binding energies measured by Hitchcock and co-workers,[46] reported as $K_1 = 291.7$ eV and $K_2 = 290.5$ eV.

In the 284.8 to 287.0 eV pre-edge region of Figure 3, bands **1** and **2** reveal vibrational progression of the excited state encompassed in each transition, shown as a series of dashed grey curves in Figure 3. The electronic states contributing to the band **1**, according to the RASPT2 calculation, are obtained at 285.68 eV and 285.95, and the electronic state centered at 286.51 eV corresponds to the band marked as **2** in Figure 3. The corresponding progression of vibrational bands are marked with a prime as 1', 1", 1'", 2' and 2" in Figure 3. Each band was deconvoluted with the same set of line shapes, and almost the same energy separation (170 and 160 meV, respectively) was preserved among the first two features. Note that our assignments stem from correlated *ab initio* calculations. At such level of theory, it is usual that multiple molecular orbital transitions contribute to a given electronic excited state. One example is the first electronic state associated with the first band in Figure 3. According to our RASPT2 results, the state is related to excitations from the C $1s$ $(2b_1)$ and $(5a_1)$ (core) occupied orbitals to the $\pi^*(2a_2)$ and $\pi^*(5b_2)$ virtual orbitals. In Table 1, we used the shorthand notation C $1s$ $(2b_1, 5a_1) \rightarrow \pi^*(2a_2, 5b_2)$. The second and third electronic states (at 285.65 and 286.51 eV) were assigned to the C $1s$ $(1b_1, 5a_1) \rightarrow \pi^*(2a_2, 5b_2)$ and C $1s$ $(2a_1) \rightarrow \pi^*(5b_2)$ states, respectively. For the carbon *K*-edge states, we also performed time-dependent density functional theory (TDDFT) calculations. The computational details of these TDDFT calculation are given in the Supplemental Information, where we also compare the TDDFT spectrum with the RASPT2 results. The TDDFT excitation energies at the carbon *K*-edge are included in Table 1. The main distinction between the TDDFT and RASPT2 results lay on the states responsible to the first band of the spectrum. RASPT2 yields two electronic states separated by 0.27 eV, whereas TDDFT produces three states separated by less than 0.1 eV. The TDDFT excitation energies were obtained at 274.58, 274.61 and 274.64 eV. The dominant contributions to these transitions are found as C $1s$ $(5a_1) \rightarrow \pi^*(5b_2)$, C $1s$ $(2b_1) \rightarrow \pi^*(2a_2)$ and C $1s$ $(1b_1) \rightarrow \pi^*(2a_2)$, i.e. transitions from the carbon atoms not bound to the chlorine (See Supporting Information for the orbital composition of each state).

Since our calculations did not include vibrational effects, it is impossible to assign the vibration progression of bands **1** and **2** based solely on our calculations, however, the vibrational progression of the carbon K-edge of chlorobenzene can be compared with the spectrum of benzene. The C $1s \rightarrow \pi^*$ excitation of benzene exhibits different vibrations with a separation of 105 (847

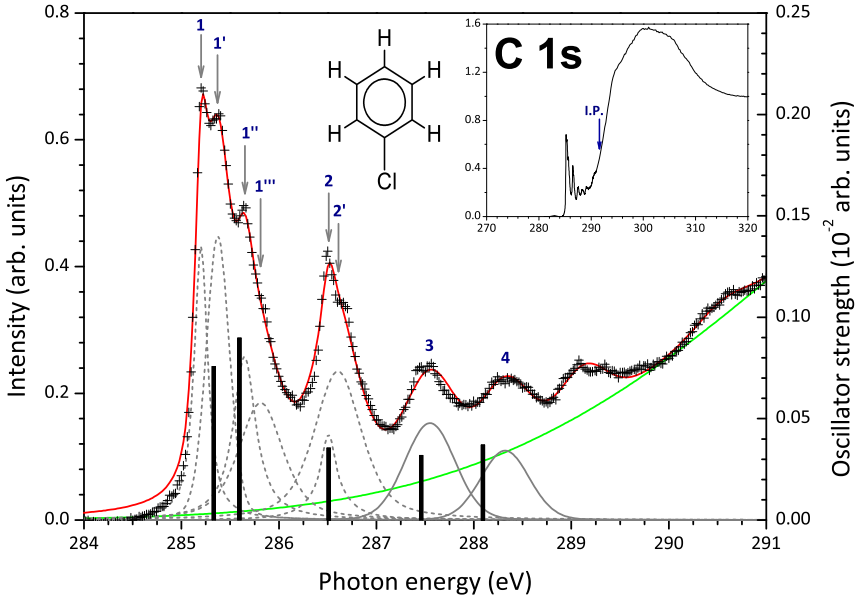


Fig. 3 NEXAFS spectrum of chlorobenzene ($C_6H_5Cl$) at the C 1*s* pre-edge region recorded by total ion yield (TIY) detection mode. The first six features were deconvoluted with Lorentzian line shapes, shown as dashed grey curves, and the center of each component is indicated by a downward arrow. Thus, the first two bands correspond to a leading transition (**1** and **2**, respectively, as shown in Table 1) and their corresponding progression of vibrational states (marked as 1', 1'', 1''' and 2'). The remaining peaks labelled as 3 and 4 were fitted with Gaussian line shapes. The continuum of states was fitted by an error step function, shown as a green curve. The top-right inset shows the NEXAFS spectrum recorded above the C 1*s* ionization limit. The vertical sticks (solid black) are centered at the excitation energies computed with the RASPT2 approach. The calculated transitions have been shifted by $-0.357$ eV to give a better correspondence with the experimental spectrum.

$cm^{-1}$), 180 (1452 $cm^{-1}$), and 420 (3388 $cm^{-1}$) meV, respectively, from the band maximum, and they have been attributed to C−H and C=C characteristic vibration modes of the benzene ring.[59] In the case of $C_6H_5Cl$, the substitution of chlorine seems to cause little effect on the vibronic excitations probed by C 1*s* excitations, mainly concentrated in the aromatic ring.

Even though band **2** has a weaker intensity than band **1**, its asymmetric shape is also an indicator of vibrational progression. The similarities with the spectrum of benzene might suggest that these features are reminiscent of the benzene structure, and only minor sensitivity to halogen substitution on the aromatic ring is observed.

### 4.2 Normal Auger spectroscopy

#### 4.2.1 Normal Auger electron emission at the carbon *K*-edge and chlorine *L*-edge

In Figure 4 the high resolution Auger electrons spectra (AES) measured by the Scienta setup are shown, together with the low resolution spectra collected with the EPICEA setup. In both cases the photon energy was kept at 350.0 eV, far above the Cl 2*p* and C 1*s* ionization thresholds in $C_6H_5Cl$. Very distinct band structures are observed in the high resolution spectra at both shells. We correlated the high resolution band structure measured with the Scienta setup with the broad structure recorded with the EPICEA. They agree reasonably well in energy position, shape and relative intensities. Both EPICEA and Scienta setups have electron energy restriction of detection: the EPICEA spectra show a fast drop in efficiency below 168.0 eV and 253.0 eV for the Cl 2*p* and C 1*s*, respectively, while the energy spectra measured by Scienta show an increase due to scattering and background contributions. Therefore, the data below these energies were not considered for analysis.

The Cl 2*p* Auger spectrum in the 165.0 eV to 183.0 eV electron kinetic energy range is shown in Figure 4 (a). Due to the spin-orbit splitting of the decaying core-hole level, the exact attribution of the Cl 2*p* Auger spectrum ($L_{2,3}VV$) is not quite so simple, and only the main bands observed are tentatively assigned.

The high-resolution Auger spectrum acquired with the Scienta setup exhibits distinct peaks that may be attributed to two progressions of bands almost equally spaced by 1.6 eV, which is in accordance with the Cl 2*p* spin-orbit splitting of 1.6 eV.[46,56,57] Therefore, these two different progressions may be interpreted as Auger electron emission following the ionization of the respective Cl $2p_{3/2}$ and $2p_{1/2}$ levels.

The C 1*s* Auger spectrum ($KVV$) of chlorobenzene in the 253.0 eV to 269.0 eV electron kinetic energy range is shown in Figure 4(b). At a first glance, the C 1*s* Auger spectrum of $C_6H_5Cl$ appears as a broad structure made up from largely unresolved bands. The C 1*s* normal Auger spectrum of the 2-chloropyrimidine molecule exhibits a similar broad band maximum at about 256 eV, due to two-hole states composed of many transitions from inner orbitals and satellites.[34] In fact, due to the similarity of the present C 1*s* normal Auger spectrum with the one measured for 2-chloropyrimidine by Storchi and co-workers,[34] it seems reasonable to state that a very large number of dicationic final states contribute to the Auger spectrum of $C_6H_5Cl$.

In the 256.0 eV to 266.0 eV electron kinetic energy range, five

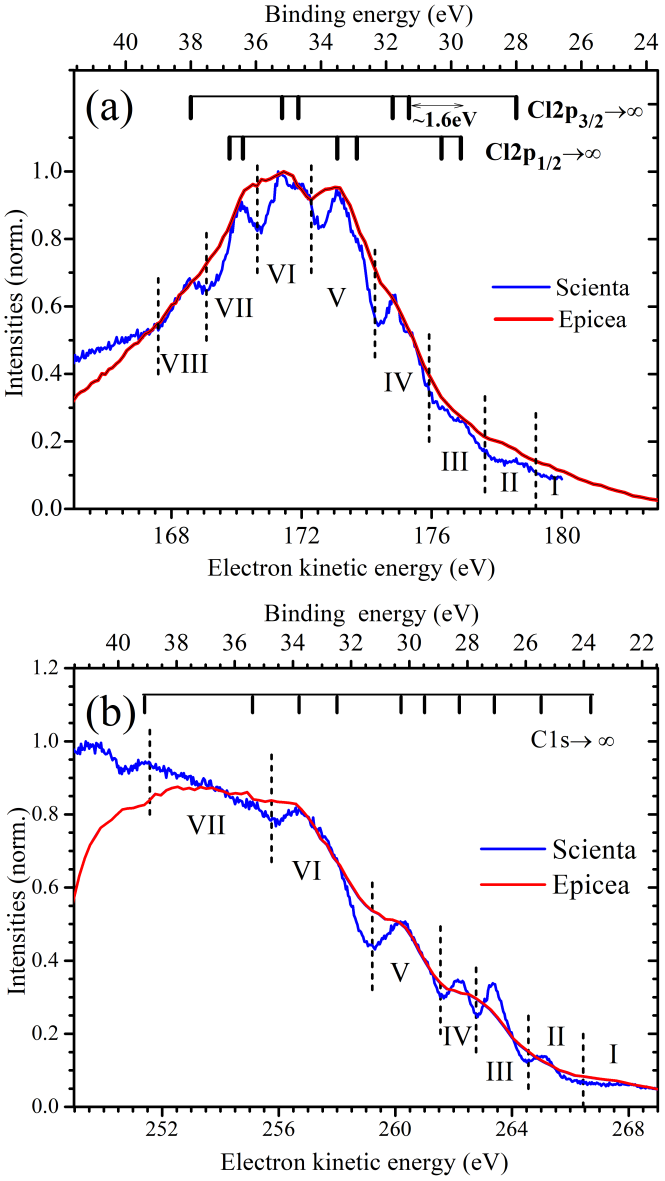


Fig. 4 (a) Cl $2p$ and (b) C $1s$ Auger spectrum of chlorobenzene acquired with 350 eV photon energy. The C $1s$ and Cl $2p$ ionization potentials were estimated as 290.4 eV and 206.7 eV by RASPT2 calculations. Vertical solid bars indicate maxima of structures in (a) and (b). In (a) correspondence of Cl $2p_{3/2}$ and Cl $2p_{1/2}$ transitions is distinguished by two individual sets of vertical bars. The electron kinetic and binding energies are collected in Table 1.

bands more distinctly resolved emerge in Figure 4 (b). Closer to the double ionization threshold, the former bands tend to be broader than the latter ones due to a higher multitude of states. As a comparison, the highest kinetic energy peak in the Auger spectrum of 2-chloropyrimidine was found at 264.0 eV, whose lowest BE was calculated to be 25.6 eV.[34] Through the sharper band at 263.4 eV electron kinetic energy, the remaining less defined bands at higher kinetic energy may suggest that the dicationic states of $C_6H_5Cl^{2+}$ are composed of fewer states. However, because of the different chemical environments for the carbon atoms (as seen in Figure 3), the C $1s$ Auger spectrum appears as the superposition of the two-hole final states reached following the decay of each nonequivalent carbons' core-hole ionization, modulated by their stoichiometry and decay rate.

For the electronic decay involving a core-hole state and two valence electrons, Auger kinetic energy may be determined by Equation (1):

$$E_K = I_C - I_i - I_j - U_{\text{eff}}(i,j) \quad (1)$$

where $E_K$ is the kinetic energy of the outgoing Auger electron, $I$ is the vertical ionization energy of the core ($C$) and valence ($i$ and $j$) electrons involved in the Auger decay and $U_{\text{eff}}(i,j)$ is the effective hole-hole interaction.[64] The dominant term in Equation (1) is the core ionization potential, which gives rise to widely spaced spectra around the inner-shells of carbon and chlorine ($KVV$ and $L_{2,3}VV$, respectively). In order to bring them into a common energy scale, the binding energy (BE) for different molecular states was estimated by taking the difference between the core level ionization energy ($I_C$) and the outgoing Auger electron kinetic energy ($E_K$), thus rearranging Equation (1) in the form $BE = I_C - E_K$. The C $1s$ and Cl $2p$ ionization potentials ($I_C$) were taken as 290.4 eV and 206.7 eV based on RASPT2 calculations. The computed binding energies are shown at the upper X-axis of Figure 4 (a) and (b), and the values derived for the main peaks are summarized in Table 2.

The BEs derived for the most intense peaks of the Cl $2p$ and C $1s$ Auger spectra of $C_6H_5Cl$ lie within the range of 28.1 eV to 38.1 eV and 24.7 eV to 39.0 eV, respectively, as shown in Table 2. The only measurements of the BE of chlorobenzene dications available in the literature[65] for comparison come from double-ionization charge transfer spectrometry, where the dication formation is indirectly probed by the double electron capture (DEC) reaction $OH^+ + C_6H_5Cl \rightarrow OH^- + C_6H_5Cl^{2+}$. Peaks were observed in the spectrum of $OH^-$ ions as a function of the $OH^+$ energy at positions, which correspond to double ionization energies of excited states of $C_6H_5Cl^{2+}$ populated in the DEC reactions. The double ionization energies (DIEs) determined by DCT for the ground (25.6 ± 0.6 eV) and four excited states of the dication $C_6H_5Cl^{2+}$ were (26.8 ± 0.3, 28.4 ± 0.3, 30.2 ± 0.6 and 32.3 ± 0.4 eV),[65] all DIEs lying in the energy range of the present Auger spectra. All the dicationic states measured by DCT are likely to be triplet states,[65] and so the present corresponding Auger peaks must also be triplets. The BEs estimated in the present work are also comparable to the lowest double ionization threshold for the closely-related benzene dication $C_6H_6{}^{2+}$, which was experimentally determined as 24.65 eV[66] and theoretically predicted to be 23.34 eV[67] (and more recently 24.25 eV[68]).

One of the major goals of the present investigation was to extract ion-correlated Auger spectra and ion's mass appearance spectra corresponding to final dicationic states in the energy domain of the different edges. We separated both spectra, the Cl $2p$ and C $1s$ AES, into eight and seven regions, respectively, following the band structures more clearly defined in the Scienta AES. The regions can be assigned to dicationic binding energy (BE) ranges and are identified by Roman numerals in Figure 4. In the low BE regions (I and II), the band structures are rather spread out and weak while the next ones, higher in binding energies, are much

Table 2 Kinetic energy and binding energy (BE) of the main features assigned in the C 1$s$ ($KVV$) and Cl 2$p$ ($L_{2,3}VV$) Auger spectra of chlorobenzene (Figure 4). The BE values were attributed assuming core ionization energies of 290.4 eV and 206.7 eV (RASPT2 calculations) in agreement with those reported in Ref. 46. The initial state vacancies ($KVV$) and ($L_{2,3}VV$) were correlated to the regions labelled (II-VIII) in Figure 4

| **Initial state vacancy** | **Electron kinetic energy/** eV | **Binding energy/** eV | **Region** |
|---|---|---|---|
| Carbon | | | |
| $K$ | 265.7 | 24.7 | II |
| $K$ | 265.0 | 25.4 | II |
| $K$ | 263.4 | 27.0 | III |
| $K$ | 262.2 | 28.2 | IV |
| $K$ | 261.2 | 29.4 | V |
| $K$ | 260.2 | 30.2 | V |
| $K$ | 257.7 | 32.7 | VI |
| $K$ | 256.7 | 33.7 | VI |
| $K$ | 255.1 | 35.3 | VII |
| $K$ | 251.4 | 39.0 | VII |
| Chlorine | | | |
| $L_3$ | 178.6 | 28.1 | II |
| $L_3$ | 176.9 | 29.8 | III |
| $L_3$ | 176.3 | 30.4 | III |
| $L_2$ | 175.3 | 31.4 | IV |
| $L_2$ | 174.8 | 31.9 | IV |
| $L_3$ | 173.7 | 33.0 | V |
| $L_3$ | 173.1 | 33.6 | V |
| $L_2$ | 171.9 | 34.8 | VI |
| $L_2$ | 171.4 | 35.3 | VI |
| $L_3$ | 170.2 | 36.5 | VII |
| $L_3$ | 168.6 | 38.1 | VIII |
| C edge ionization energies | | | |
| RASPT2: | | | |
| C 1$s$ ($5a_1$) | 290.36 | | |
| C 1$s$ ($2b_1$) | 290.90 | | |
| C 1$s$ ($4a_1$) | 291.17 | | |
| C 1$s$ ($1b_1$) | 291.23 | | |
| C 1$s$ ($3a_1$) | 291.58 | | |
| C 1$s$ ($2a_1$) | 291.99 | | |
| Cl 2$p$ edge ionization energies | | | |
| RASPT2: | | | |
| Cl $2p_{3/2}$ | 206.6 | | |
| Cl $2p_{3/2}$ | 206.7 | | |
| Cl $2p_{1/2}$ | 208.2 | | |

more defined and intense. It is reasonable to suggest that the density of states should be smaller at these energy regions than at the next ones. At the intermediate and high BE regions, from III up to VII (or VIII for the Cl 2$p$), the bands are more discernible and pronounced. Even though, the larger peaks seem to be composed by at least double and multiple structures. At these energy ranges, the density of states certainly increases and many dicationic states contribute to each single band/structure observed in the spectrum. Among these latter signals, in the Cl 2$p$ AES, the bands present similar shapes. In contrast, in the C 1$s$ AES, the band shapes tend to broaden increasing in binding energy. Similar trends were observed in the Auger spectra of benzene.[67] Assignments of the energetic ordering and character of the double ionization states are surely hampered by the complex transitions resulting from the high density of dicationic states.As the knowledge of individual states was not feasible, the averaging approach presented here by sectioning the Auger electron spectra in regions composed of groups of states is used for the qualitative discussion of the ion-mass correlated binding energy observations.

#### 4.2.2 Auger electron-ion coincidence spectra

Measuring the energy-resolved electrons in coincidence with the cations resulting from the initial Cl 2$p$ and C 1$s$ ionization can provide deeper insights into the ions' formation in the Auger process. Therefore, we correlated the ion-TOF spectra with the Epicea-AES. The analysis followed two approaches: (1) extract the AES spectrum in correspondence to dicationic species and discriminate the band structures of the total AES spectrum leading to dicationic ions; (2) extract all formed ionic species by the band structures of the AES spectrum.

It is already known that electron impact ionization at the low to intermediate energy range (30-2000 eV), proton impact at 150 eV and $OH^-$ charge-exchange collisions lead to the formation of metastable dications.[35,36,65] Prompted by these previous findings, we searched again here for these dicationic species. Un-

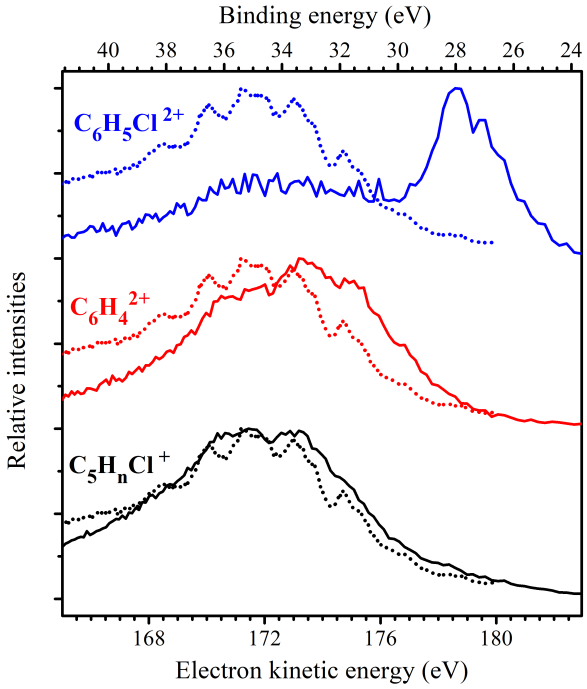


Fig. 5 Metastable dications $C_6H_5Cl^{2+}$ and $C_6H_4{}^{2+}$ and fragment single-charged species $C_6H_nCl^+$ Auger electron spectra in the Cl $2p$ energy region, produced by 350 eV photons. The total Auger spectrum is superimposed as dashed line for comparison. All spectra were normalized to unity at highest intensity for better shape and electron kinetic energy position evaluation.

expectedly, very pronounced, well defined, peaks emerged in the ion-TOF spectra even under photo ionization-excitation in the energy domain of the Cl $2p$ and the C $1s$ edges.

Figures 5, 6 and 7 show the ion-correlated Auger electron spectra — with the binding energies indicated at the upper abscissa axis — for three representative ionic species, namely the doubly charged species $C_6H_5Cl^{2+}$ and $C_6H_4{}^{2+}$, and the singly charged $C_5H_nCl^+$ ($n$=1–5) fragments (solid lines). From the multiparameter data, Auger kinetic energy spectra were extracted setting coincidence time of flight (mass/charge) windows in the ion-TOF spectra (Mass selected Auger Electron Spectra (MS-AES). The MS-AES intensities were, for each individual species, normalized to unity for position and shape comparison. The total Auger electron spectra were superimposed as dashed lines for a better evaluation of the positions of the band structures. All distributions were normalized to unity at their maximum intensities and therefore are not in scale. As can be seen from the figures, the binding energies involved in the formation of $C_6H_5Cl^{2+}$ at both shells, Cl $2p$ and C $1s$, are within the same energy range (Figures 5 and 6, respectively), indicating that a specific energy window from 25 up to 30 eV is required to promote the system into the double charged parent ion, which is metastable.

In Figure 7 we combined, in a binding energy scale, the MS-AES distributions at the Cl $2p$ and C 1s shells for easy of comparison. From this figure it can be seen that the binding energy range for the $C_6H_5Cl^{2+}$ dication is well defined by a peaked structure with maximum around 28 eV. In this figure we indicate by vertical bars the energy maxima extracted from the SCIENTA photoelectron spectra (Figure 4), for the Cl $2p$ (dashed line) and C $1s$ (solid line) edges ionization, leading to $C_6H_5Cl^{2+}$ formation. These energy maxima are in good agreement with those previously determined by ion impact experiments.[65] These data were included in Figure 7 at the upper x-abscissa by black dashed lines labeled DCT (Double Charge Transfer). They correspond to the first five peaks maxima extracted from transitional energy spectra measured in double-electron-capture (DEC) reactions. Three of these maxima are within the $C_6H_5Cl^{2+}$ window and coincide with the present data. This gives us some confidence on the validity of data obtained for the other dication, $C_6H_4{}^{2+}$, to which no comparable previous data are available. It is important to notice that in the DCT experiment the ionic species were not discriminated and we associate the higher DCT maxima to both $C_6H_5Cl^{2+}$ and to $C_6H_4{}^{2+}$ formation.

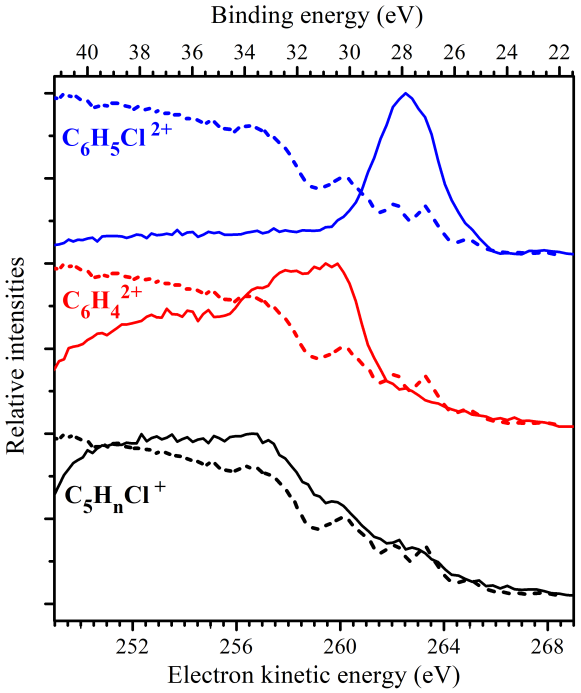


Fig. 6 Metastable dications $C_6H_5Cl^{2+}$ and $C_6H_4{}^{2+}$ and fragment single-charged species $C_6H_nCl^+$ Auger electron spectra in the C $1s$ energy region, produced by 350 eV photons. The total Auger spectrum is superimposed as dashed line for comparison. All spectra were normalized to unity at highest intensity for better shape and electron kinetic energy position evaluation.

At both shells the upper binding energy limit of $C_6H_5Cl^{2+}$ coincides with the lower binding energy limit of $C_6H_4{}^{2+}$ at around 30 eV. This evidence suggests that $C_6H_5Cl^{2+}$ decays partially into the moieties $C_6H_4{}^{2+}$ and HCl. In the case of Cl $2p$ excitation (see Figure 5), beyond the peaked structure, a broad second binding energy distribution is outlined that matches, in range and shape, that of $C_6H_4{}^{2+}$. The well defined presence of $C_6H_4{}^{2+}$ indicates that the Auger process tends to form analogue dications of the benzene skeleton. We called these species "analogue" since there is the possibility of conformational and tautomeric effects. In general, observing Figures 5 and 6, the MS-AES distribution

of $C_6H_4^{2+}$ seems to define an intermediate metastable state, its energy distribution determined between that of $C_6H_5Cl^{2+}$ and of $C_5H_nCl^+$, the single-charged fragment of the dissociating ionic pair. Again, in Figure 7 we indicate by dashed and solid vertical bars several energies maxima extracted from Figure 4, for the Cl $2p$ and C $1s$ excitations. The structures observed in the MS-AES for $C_6H_4^{2+}$ can be set in correspondence to the bands maxima of the SCIENTA spectra.

The $C_5H_nCl^+$ distribution matches the total AES distribution and shows that a high number of accessible final dissociate states is reached. Beyond a certain binding energy, all doubly dicationic final states play more important roles in breaking the excited dications into two charged moieties.

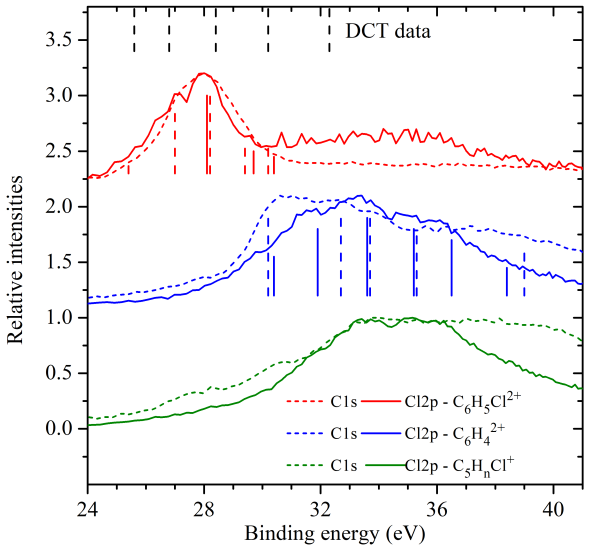


Fig. 7 Binding energy spectra at Cl $2p$ (dashed line) and C $1s$ (solid line) edge ionization of metastable dications $C_6H_5Cl^{2+}$ and $C_6H_4^{2+}$ and fragment single-charged species $C_6H_nCl^+$ produced by 350 eV photons. Vertical solid and dashed bars indicate binding energy maxima extracted from high resolution Scienta photoelectron spectra (Figure 4 (a) and (b)) for Cl $2p$ and C $1s$ edge ionization, respectively. In upper x-abscissa vertical dashed black bars indicate Double Charge Transfer data.[65] All spectra were normalized to the highest intensity in the binding energy range for better shape and binding energy position evaluation.

It should be noticed that in the previous ionization studies using charged particles[35,36] we could not disentangle the $C_3H_n^+$ and $C_6H_4^{2+}$ contributions. With the present setup, on the other hand, the dication $C_6H_4^{2+}$ was nicely discriminated by its very narrow peak in contrast to the broad ion kinetic energy distribution of $C_3H_n^+$ fragments. The peak widths of $C_6H_5Cl^{2+}$ and $C_6H_4^{2+}$ are very similar, pointing to the Maxwell Boltzmann thermal distribution.

### 4.2.3 Ion-TOF Auger electron-ion coincidence spectra

Figures 8 and 9 display the mass spectra in coincidence with energy resolved electrons (ER-mass spectra) at the calibrated binding energy regions labelled from I through VIII in Figure 4. We included on the right the Scienta BE spectra indicating the regions selected to follow the species formations. The relative intensities were normalized to the sum of all ions in each energy range.

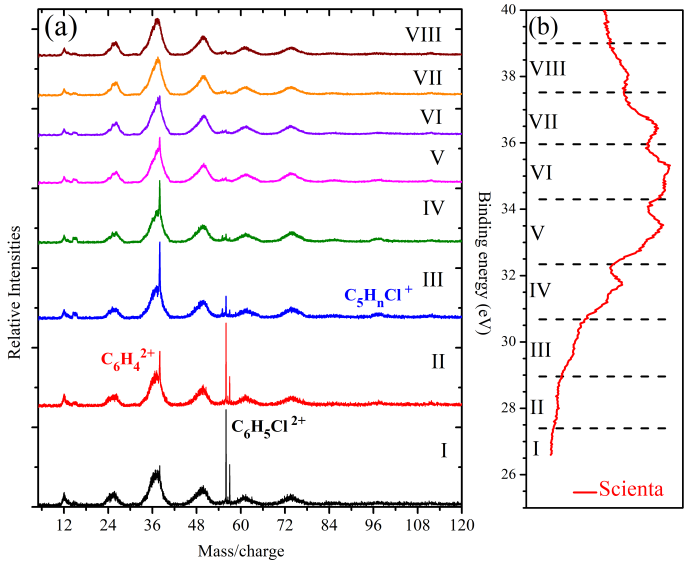


Fig. 8 (a) Relative intensities of photoelectron–photoion coincidence mass spectra (I-VIII) as function of binding energy regions (I-VIII) of the Cl $2p$ Auger electron detected. (b) Cl $2p$ Auger spectrum produced by 350 eV photons divided in eight binding energy regions (I-VIII) defined on the structures of the Auger spectrum (Figure 4 (a)).

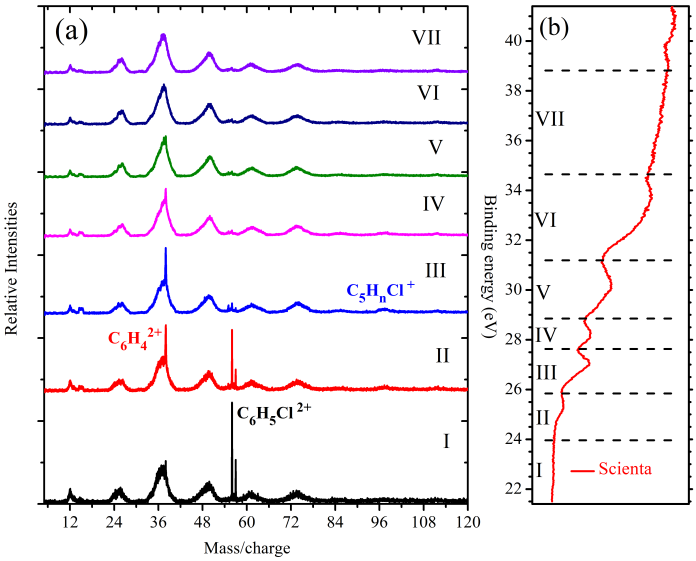


Fig. 9 (a) Relative intensities of photoelectron– photoion coincidence mass spectra (I-VII) as function of the binding energy regions (I-VII) of the C $1s$ Auger electron detected. (b) C $1s$ electron Auger spectrum produced by 350 eV photons divided in seven binding energy regions ((I-VII) defined on the structures of the Auger spectra (Figure 4 (b)).

The ion-TOF distributions show very clearly that the production of the dicationic metastable species depends on the binding energy ranges or populated final states. These species are easily discernible, as they appear as very narrow peaks, clearly identifiable in the spectra. In the normal Auger processes started with the Cl 2*p* and C 1*s* excitation, the first four and three regions (bands), respectively, give rise to the parent molecular dication. Not only $C_6H_5Cl^{2+}$, but also $C_6H_4{}^{2+}$, are observed with significant intensity.

In the case of Cl 2*p* excitation, it is only when the relative intensity of $C_6H_5Cl^{2+}$ at regions III and IV becomes comparatively very weak, that the $C_6H_4{}^{2+}$ production strongly enhances, disappearing afterwards at region VI. This behavior may again indicate that $C_6H_5Cl^{2+}$ decays into $C_6H_4{}^{2+}$. Together with the reduction of the parent dication production moving towards region III, a narrow peak arises on the low mass side of $C_6H_5Cl^{2+}$. The ER-mass spectra show here the weak opening of the dehydrogenation dicationic channel $C_6H_4Cl^{2+}$. All other peaks are composed of ionic single charged species originated from dissociative double charged states. On the other hand, in the C 1*s* excitation the relative intensity of the parent molecular dication is already at its maximum in region I and very faint at region III, and $C_6H_4{}^{2+}$ intensity starts to increase in region I, disappearing in region V. The appearance of the $C_6H_4Cl^{2+}$ is noted at region III, but its presence becomes promptly very weak at region IV.

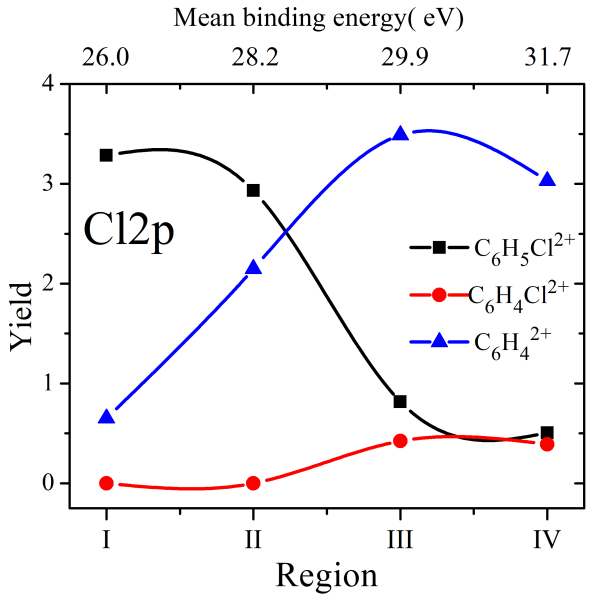


Fig. 10 Yields of selected dications $C_6H_5Cl^{2+}$, $C_6H_4Cl^{2+}$ and $C_6H_4{}^{2+}$ extracted from ion-mass spectra (I-IV) (Figure 8) obtained from Cl 2*p* Auger energy regions, produced by 350 eV photons. Mean binding energy of binding energy regions (I-IV) determined from figure 4 (a) indicated on the upper x-abscissa.

In order to get a quantitative evaluation of the ions formation, we extracted yields of the metastable species relative to the sum of all dissociating species as shown in figures 10 and 11 as function of the energy region and correlated BE ranges. At the upper x abscissa we added the weighted mean binding energy of each energy region. From these figures it is easier to evaluate similarities

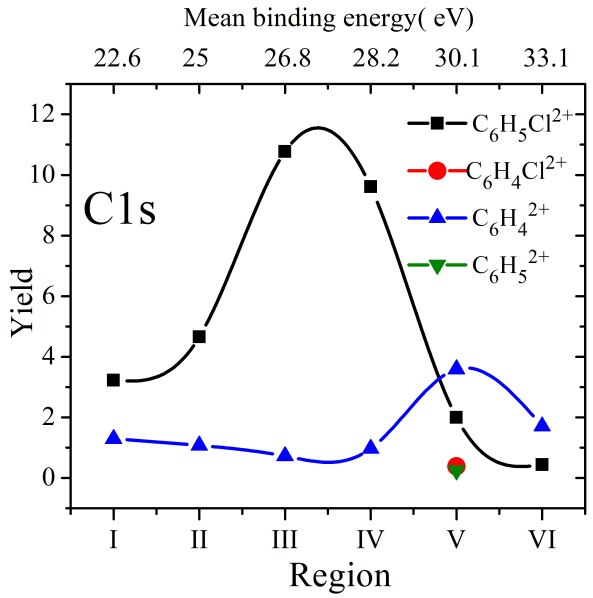


Fig. 11 Yields of selected dications $C_6H_5Cl^{2+}$, $C_6H_4Cl^{2+}$, $C_6H_5{}^{2+}$ and $C_6H_4{}^{2+}$ extracted from ion-mass spectra (I-VI) (Figure 9) obtained from C 1*s* Auger energy regions, produced by 350 eV photons. Mean binding energy of binding energy regions (I-VI) determined from figure 4 (b) indicated on the upper x-abscissa.

and discrepancies of the relative intensities at both edges initial excitation. From the distributions it seems that the maximum yield of $C_6H_5Cl^{2+}$ occurs more clearly around 27.0 eV. Figure 11 depicts the enhancement and decrease at the C 1*s* excitation of $C_6H_5Cl^{2+}$ production, which is not shown at the Cl 2*p* due to the selection of a narrower energy range.

At both shells the formation of $C_6H_4{}^{2+}$ depicts a maximum slightly above 30 eV. In the case of the C 1*s* it reaches only 1/4 of the $C_6H_5Cl^{2+}$ yield, while it supersedes at the Cl 2*p* excitation. Only very low yields were measured for $C_6H_5{}^{2+}$ and $C_6H_4Cl^{2+}$ at the C 1*s* shell, but at the Cl 2*p* shell $C_6H_4Cl^{2+}$ the full yield dependency was measured peaking around 31 eV. Here it becomes clear from the maxima evaluation, that similar excited final states might being populated, but their strengths strongly dependent on the initial shell ionization. Comparison of the binding energy widths of the individual dications formed by Cl 2*p* and C 1*s* excitation shows that the widths of the former process are wider than those of the latter. This observation might be correlated to the presence of two spin states' populations, namely spin 1/2 and 3/2 states, absent in the C 1*s* case.

## 5 Summary and Conclusions

NEXAFS, Normal Auger and ion-TOF spectra of chlorobenzene were recorded at 350 eV photons above the C 1*s* and Cl 2*p* edges, employing soft X-ray synchrotron radiation provided by the high-resolution beamline PLÉIADES at Synchrotron SOLEIL.

The *ab initio* RASPT2 approach was used to compute core excited/ionized states of chlorobenzene including spin-orbit coupling effects in the inner-shell excitation/ionization of the Cl 2*p*. Comparison of theoretical results and NEXAFS spectra allowed for a reliable assignment of the electronic transitions.

High-resolution energy Auger spectra discriminated the binding energy (BEs) regions for several molecular states. These spectra were superimposed to less resolved Epicea spectra, which were used for correlating the electron kinetic energy and equivalent BE distributions to the metastable and dicationic fragments' production. A pronounced binding energy selectivity in the metastable dications' formation was observed, in contrast with the behaviour of a singly ionized fragment generated by fast pair dissociation. The electron kinetic energy distribution of the latter is very similar to the total electrons distribution. For the metastable dicationic production, ion-mass spectra correlated with the binding energy regions showed clearly the contribution mainly of fast Auger electrons and equivalently defined binding energy windows. A selectivity of the carbon or chlorine atom in the production of dicationic species was not observed as the C 1*s* and Cl 2*p* excitations form metastable double charged species as well as single charged pair fragments. The spin-orbit character of the Cl 2*p* transition states may define larger BE's windows for the fragment species production than the C 1*s* states. The mean binding energy windows suggest that analogue benzene dications may arise from the decay of the molecular clorobenzene dication. An absolute qualitative contribution of C 1*s* and Cl 2*p* normal Auger process in the metastable species production is still an open question.

## Conflicts of interest

There are no conflicts to declare.

## Acknowledgements

This work was performed on the PLÉIADES beamline at the SOLEIL Synchrotron under Proposal No. 20170006. We acknowledge SOLEIL for provision of high quality synchrotron radiation facilities and thank the PLÉIADES beamline team for their assistance. B.T. and S.C. acknowledge support from the Independent Research Fund Denmark–Natural Sciences, DFF-RP2 grant No. 7014-00258B and from the European Union's Horizon 2020 Research and Innovation Programme under the Marie Skłodowska-Curie Individual Fellowship, grant agreement 101027796.

## Notes and references

1 C. Miron and P. Morin, *Nuclear Instruments and Methods in Physics Research A*, 2009, **601**, 66–77.

2 P. Salén, L. Schio, R. Richter, M. Alagia, S. Stranges and V. Zhaunerchyk, *Phys. Rev. A*, 2020, **102**, 032817.

3 M. Gerlach, F. Fantuzzi, L. Wohlfart, K. Kopp, B. Engels, J. Bozek, C. Nicolas, D. Mayer, M. Gühr, F. Holzmeier and I. Fischer, *J. Chem. Phys.*, 2021, **154**, 114302.

4 H. Iwayama, N. Sisourat, P. Lablanquie, F. Penent, J. Palaudoux, L. Andric, J. H. D. Eland, K. Bučar, M. Žitnik, Y. Velkov, Y. Hikosaka, M. Nakano and E. Shigemasa, *J. Chem. Phys.*, 2013, **138**, 024306.

5 S. Zagorodskikh, J. H. D. Eland, V. Zhaunerchyk, M. Mucke, R. J. Squibb, P. Linusson and R. Feifel, *J. Chem. Phys.*, 2016, **145**, 124302.

6 H. Levola, E. Itälä, K. Schlesier, K. Kooser, S. Laine, J. Laksman, D. T. Ha, E. Rachlew, M. Tarkanovskaja, K. Tanzer and E. Kukk, *Phys. Rev. A*, 2015, **92**, 063409.

7 J. H. D. Eland, P. Linusson, M. Mucke and R. Feifel, *Chem. Phys. Lett.*, 2012, **548**, 90–94.

8 H. Fukuzawa, G. Prümper, X. Liu, E. Kukk, R. Sankari, M. Hoshino, H. Tanaka, Y. Tamenori and K. Ueda, *Chem. Phys. Lett.*, 2007, **436**, 51–56.

9 K. Le Guen, M. Ahmad, D. Céolin, P. Lablanquie, C. Miron, F. Penent, P. Morin and M. Simon, *J. Chem. Phys.*, 2005, **123**, 084302.

10 C. Miron, M. Simon, N. Leclercq, D. L. Hansen and P. Morin, *Phys. Rev. Lett.*, 1998, **81**, 4104–4107.

11 B. N. C. Tenorio, R. R. Oliveira and S. Coriani, *Chem. Phys.*, 2021, **548**, 111226.

12 A. C. F. Santos, D. N. Vasconcelos, M. A. MacDonald, M. M. Sant'Anna, B. N. C. Tenório, A. B. Rocha, V. Morcelle, N. Appathurai and L. Zuin, *J. Chem. Phys.*, 2018, **149**, 054303.

13 V. Morcelle, A. Medina, L. C. Ribeiro, I. Prazeres, R. R. T. Marinho, M. S. Arruda, L. A. V. Mendes, M. J. Santos, B. N. C. Tenório, A. Rocha and A. C. F. Santos, *J. Phys. Chem. A*, 2018, **122**, 9755–9760.

14 X. J. Liu, G. Prümper, E. Kukk, R. Sankari, M. Hoshino, C. Makochekanwa, M. Kitajima, H. Tanaka, H. Yoshida, Y. Tamenori and K. Ueda, *Physical Review A - Atomic, Molecular, and Optical Physics*, 2005, **72**, 042704.

15 Y.-S. Lin, C.-C. Tsai, H.-R. Lin, T.-L. Hsieh, J.-L. Chen, W.-P. Hu, C.-K. Ni and C.-L. Liu, *J. Phys. Chem. A*, 2015, **119**, 6195–6202.

16 Z. Li, L. Inhester, C. Liekhus-Schmaltz, B. F. E. Curchod, J. W. Snyder, N. Medvedev, J. Cryan, T. Osipov, S. Pabst, O. Vendrell, P. Bucksbaum and T. J. Martinez, *Nature Communications*, 2017, **8**, 453.

17 S. Oberli, J. González-Vázquez, E. Rodríguez-Perelló, M. Sodupe, F. Martín and A. Picón, *Phys. Chem. Chem. Phys.*, 2019, **21**, 25626–25634.

18 A. Picón, C. S. Lehmann, C. Bostedt, A. Rudenko, A. Marinelli, T. Osipov, D. Rolles, N. Berrah, C. Bomme, M. Bucher, G. Doumy, B. Erk, K. R. Ferguson, T. Gorkhover, P. J. Ho, E. P. Kanter, B. Krässig, J. Krzywinski, A. A. Lutman, A. M. March, D. Moonshiram, D. Ray, L. Young, S. T. Pratt and S. H. Southworth, *Nature Communications*, 2016, **7**, 11652.

19 Y. J. Chiang, Y. S. Lin, H. R. Lin and C. L. Liu, *Chem. Phys. Lett.*, 2018, **706**, 215–222.

20 E. Itälä, H. Levola, D. T. Ha, K. Kooser, E. Rachlew and E. Kukk, *J. Phys. Chem. A*, 2016, **120**, 5419–5426.

21 E. Itälä, D. T. Ha, K. Kooser, M. A. Huels, E. Rachlew, E. N. ommiste, U. Joost and E. Kukk, *Journal of Electron Spectroscopy and Related Phenomena*, 2011, **184**, 119–124.

22 P. Bolognesi, J. A. Kettunen, A. Cartoni, R. Richter, S. Tosic, S. Maclot, P. Rousseau, R. Delaunay and L. Avaldi, *Phys. Chem. Chem. Phys.*, 2015, **17**, 24063–24069.

23 P. Bolognesi, P. O'Keeffe, Y. Ovcharenko, M. Coreno, L. Avaldi, V. Feyer, O. Plekan, K. C. Prince, W. Zhang and V. Carravetta, *J. Chem. Phys.*, 2010, **133**, 034302.

24 E. Kukk, D. T. Ha, Y. Wang, D. G. Piekarski, S. Diaz-Tendero, K. Kooser, E. Itälä, H. Levola, M. Alcamí, E. Rachlew and F. Martín, *Phys. Rev. A*, 2015, **91**, 043417.

25 T. Kierspel, C. Bomme, M. Di Fraia, J. Wiese, D. Anielski, S. Bari, R. Boll, B. Erk, J. S. Kienitz, N. L. M. Müller, D. Rolles, J. Viefhaus, S. Trippel and J. Küpper, *Phys. Chem. Chem. Phys.*, 2018, **20**, 20205–20216.

26 B. N. Cabral Tenorio, F. Kruczkiewicz, F. de Almeida Ribeiro, D. P. Pinho Andrade, H. M. Riani de Luna, H. M. Boechat-Roberty, M. A. C. Nascimento, A. B. Rocha and W. Wolff, *J. Phys. Chem. A*, 2019, **123**, 1389–1398.

27 M. H. Palmer, T. Ridley, S. Vrønning Hoffmann, N. C. Jones, M. Coreno, M. de Simone, C. Grazioli, T. Zhang, M. Biczysko, A. Baiardi and K. A. Peterson, *J. Chem. Phys.*, 2016, **144**, 124302.

28 R. Bohinc, M. Žitnik, K. Bučar, M. Kavčič, S. Carniato, L. Journel, R. Guillemin, T. Marchenko, E. Kawerk, M. Simon and W. Cao, *J. Chem. Phys.*, 2016, **144**, 134309.

29 O. Plekan, M. Coreno, V. Feyer, A. Moise, R. Richter, M. D. Simone, R. Sankari and K. C. Prince, *Physica Scripta*, 2008, **78**, 058105.

30 Y.-S. Lin, K.-T. Lu, Y. T. Lee, C.-M. Tseng, C.-K. Ni and C.-L. Liu, *J. Phys. Chem. A*, 2014, **118**, 1601–1609.

31 L. Schwob, S. Dörner, K. Atak, K. Schubert, M. Timm, C. Bülow, V. Zamudio-Bayer, B. von Issendorff, J. T. Lau, S. Techert and S. Bari, *J. Phys. Chem. Lett.*, 2020, **11**, 1215–1221.

32 Y.-S. Lin, H.-R. Lin, W.-L. Liu, Y. T. Lee, C.-M. Tseng, C.-K. Ni, C.-L. Liu, C.-C. Tsai, J.-L. Chen and W.-P. Hu, *Chem. Phys. Lett.*, 2015, **636**, 146–153.

33 P. Bolognesi, P. O'Keeffe, Y. Ovcharenko, L. Avaldi and V. Carravetta, *J. Chem. Phys.*, 2012, **136**, 154308.

34 L. Storchi, F. Tarantelli, S. Veronesi, P. Bolognesi, E. Fainelli and L. Avaldi, *J. Chem. Phys.*, 2008, **129**, 154309.

35 W. Wolff, A. Perlin, R. R. Oliveira, F. Fantuzzi, L. H. Coutinho, F. de A Ribeiro and G. Hilgers, *J. Phys. Chem. A*, 2020, **124**, 9261–9271.

36 F. Fantuzzi, B. Rudek, W. Wolff and M. A. C. Nascimento, *J. Am. Chem. Soc.*, 2018, **140**, 4288–4292.

37 Y.-J. Chiang, W.-C. Huang, C.-K. Ni, C.-L. Liu, C.-C. Tsai and W.-P. Hu, *AIP Advances*, 2019, **9**, 085023.

38 P.-Å. Malmqvist, K. Pierloot, A. R. M. Shahi, C. J. Cramer and L. Gagliardi, *J. Chem. Phys.*, 2008, **128**, 204109.

39 V. Sauri, L. Serrano-Andrés, A. R. M. Shahi, L. Gagliardi, S. Vancoillie and K. Pierloot, *J. Chem. Theory Comput.*, 2011, **7**, 153–168.

40 M. Q. AlKhaldi and R. Wehlitz, *J. Chem. Phys.*, 2016, **144**, 044304.

41 `https://www.synchrotron-soleil.fr/fr/lignes-de-lumiere/pleiades`.

42 P. Morin, M. Simon, C. Miron, N. Leclercq and D. Hansen, *Journal of Electron Spectroscopy and Related Phenomena*, 1998, **93**, 49–60.

43 X.-J. Liu, C. Nicolas and C. Miron, *Review of Scientific Instruments*, 2013, **84**, 033105.

44 T. D. Thomas and R. W. Shaw, *Journal of Electron Spectroscopy and Related Phenomena*, 1974, **5**, 1081–1094.

45 M. Kato, Y. Morishita, M. Oura, H. Yamaoka, Y. Tamenori, K. Okada, T. Matsudo, T. Gejo, I. Suzuki and N. Saito, *J. Electron Spectrosc. Relat. Phenomena*, 2007, **160**, 39–48.

46 A. P. Hitchcock, M. Pocock, C. E. Brion, M. S. Banna, D. C. Frost, C. A. McDowell and B. Wallbank, *Journal of Electron Spectroscopy and Related Phenomena*, 1978, **13**, 345–360.

47 B. O. Roos, P. R. Taylor and P. E. M. Siegbahn, *Chem. Phys.*, 1980, **48**, 157–173.

48 J. Olsen, B. O. Roos, P. Jørgensen and H. J. A. Jensen, *J. Chem. Phys.*, 1988, **89**, 2185–2192.

49 P. A. Malmqvist, A. Rendell and B. O. Roos, *J. Phys. Chem.*, 1990, **94**, 5477–5482.

50 M. G. Delcey, L. K. Sørensen, M. Vacher, R. C. Couto and M. Lundberg, *J. Comput. Chem.*, 2019, **40**, 1789–1799.

51 B. O. Roos, R. Lindh, P.-A. Malmqvist, V. Veryazov and P.-O. Widmark, *J. Phys. Chem. A*, 2004, **108**, 2851–2858.

52 P. Å. Malmqvist, *Int. J. Quantum Chem.*, 1986, **30**, 479–494.

53 P. Å. Malmqvist, B. O. Roos and B. Schimmelpfennig, *Chemical Physics Letters*, 2002, **357**, 230–240.

54 P.-Å. Malmqvist and B. O. Roos, *Chem. Phys. Lett.*, 1989, **155**, 189–194.

55 *NIST Chemistry WebBook – Standard Reference Database Number 69*, 2021, `https://doi.org/10.18434/T4D303`.

56 A. Barrie, I. Drummond and Q. Herd, *Journal of Electron Spectroscopy and Related Phenomena*, 1974, **5**, 217–225.

57 A. A. Bakke, H.-W. Chen and W. L. Jolly, *Journal of Electron Spectroscopy and Related Phenomena*, 1980, **20**, 333–366.

58 M. X. Yang, M. Xi, H. Yuan, B. E. Bent, P. Stevens and J. White, *Surface Science*, 1995, **341**, 9–18.

59 E. E. Rennie, B. Kempgens, H. M. Köppe, U. Hergenhahn, J. Feldhaus, B. S. Itchkawitz, A. L. D. Kilcoyne, A. Kivimäki, K. Maier, M. N. Piancastelli, M. Polcik, A. Rüdel and A. M. Bradshaw, *J. Chem. Phys.*, 2000, **113**, 7362–7375.

60 M. L. Vidal, M. Epshtein, V. Scutelnic, Z. Yang, T. Xue, S. R. Leone, A. I. Krylov and S. Coriani, *J. Phys. Chem. A*, 2020, **124**, 9532–9541.

61 A. Hitchcock and C. Brion, *Journal of Electron Spectroscopy and Related Phenomena*, 1977, **10**, 317–330.

62 J. A. Horsley, J. Stöhr, A. P. Hitchcock, D. C. Newbury, A. L. Johnson and F. Sette, *J. Chem. Phys.*, 1985, **83**, 6099–6107.

63 I. L. Bradeanu, R. Flesch, N. Kosugi, A. A. Pavlychev and E. Rühl, *Phys. Chem. Chem. Phys.*, 2006, **8**, 1906–1913.

64 D. R. Jennison, *Phys. Rev. A*, 1981, **23**, 1215–1222.

65 F. M. Harris, P. J. Jackson, J. A. Rontree and W. J. Griffiths, *Organic Mass Spectrometry*, 1992, **27**, 261–269.

66 J. H. Eland, *Chem. Phys.*, 2008, **345**, 82–86.

67 F. Tarantelli, A. Sgamellotti, L. S. Cederbaum and J. Schirmer, *J. Chem. Phys.*, 1987, **86**, 2201–2206.

68 G. Zhao, T. Miteva and N. Sisourat, *Eur. Phys. J. D*, 2019, **73**, 69.